Simultaneous SPECT imaging with ^{123}I and ^{125}I - a practical approach to assessing a drug and its carrier at the same time with dual imaging

Zeynab Nosrati [a], Pedro L. Esquinas [b], Cristina Rodríguez-Rodríguez [a,c], Thuy Tran [d], Anil Maharaj [a], Katayoon Saatchi [a,*], Urs O. Häfeli [a,d,*]

[a] *Faculty of Pharmaceutical Sciences, University of British Columbia, 2405 Wesbrook Mall, Vancouver, British Columbia V6T 1Z3, Canada*
[b] *IBM Watson Health Imaging, 6303 Airport Road, Mississauga, Ontario, L4V 1R8 Canada*
[c] *Department of Physics and Astronomy, University of British Columbia, 6224 Agricultural Road, Vancouver, British Columbia V6T 1Z1, Canada*
[d] *Department of Pharmacy, Faculty of Health and Medical Sciences, University of Copenhagen, Copenhagen 2100, Denmark*

ARTICLE INFO

ABSTRACT

Radiolabeling of a drug with radioactive iodine is a good method to determine its pharmacokinetics and bio-distribution *in vivo* that only minimally alters its physicochemical properties. With dual labeling, using the two radioactive iodine isotopes ^{123}I and ^{125}I, two different drugs can be evaluated at the same time, or one can follow both a drug and its drug delivery system using a single photon emission computed tomography (SPECT) imager. One difficulty is that the two radioisotopes have overlapping gamma spectra. Our aim was therefore to develop a technique that overcomes this problem and allows for quantitative analysis of the two radioisotopes present at varied isotope ratios. For this purpose, we developed a simple method that included scatter and attenuation corrections and fully compensated for ^{123}I/^{125}I crosstalk, and then tested it in phantom measurements. The method was applied to the study of an orally administered lipid formulation for the delivery of fenofibrate in rats. To directly compare a traditional study, where fenofibrate was determined in plasma samples to SPECT imaging with ^{123}I-labeled fenofibrate and ^{125}I-labeled triolein over 24 h, the drug concentrations were converted to standardized uptake values (SUVs), an unusual unit for pharmaceutical scientists, but the standard unit for ra-diologists. A generally good agreement between the traditional and the radioactive imaging method was found in the pharmacokinetics and biodistribution results. Small differences are discussed in detail. Overall, SPECT im-aging is an excellent method to pilot a new formulation with just a few animals, replaces blood sampling, and can very quickly highlight potential administration problems, the excretion pathways and the kinetics. Furthermore, dual labeling with the two radioisotopes ^{123}I and ^{125}I clearly shows if a drug and its drug delivery system stay together when traveling through the body, if slow drug release takes place, and where degradation/excretion of the components occurs.

1. Introduction

Preclinical imaging, which forms a translational bridge from cells to animals to the clinical environment, plays an important role in improving, accelerating and reducing cost in drug discovery and development (Rudin and Weissleder, 2003; Vanderheyden, 2009). By means of preclinical imaging, clinically relevant longitudinal studies can be designed in a single animal and predict the clinical efficacy of new drugs before moving to human testing (Willmann et al., 2008).

Single-photon emission computed tomography (SPECT), a sensitive radionuclide-based imaging modality, has been extensively used as a valuable tool in drug discovery and development, ranging from pre-clinical research to early clinical trials (Perkins and Frier, 2004). In preclinical studies, a small animal SPECT based camera, scaled down from a clinical SPECT system, is a valuable tool for molecular imaging and tracking radiolabeled drug molecules (Gomes et al., 2011). In this way, the *in vivo* distribution, pharmacokinetics and targeting properties of drugs, biologics, nanomedicines and innovative drug delivery systems can be examined closely and quantitatively.

In modern drug delivery systems, the drug does not always behave like the drug carrier, and observing their differences at the same time might be enormously helpful to optimize the drug formulation and the

---

* Corresponding authors.
  E-mail addresses: kathy.saatchi@ubc.ca (K. Saatchi), urs.hafeli@ubc.ca (U.O. Häfeli).

drug delivery process. SPECT is a technique that allows for simultaneous imaging of two (or more) radionuclides based on their distinct gamma energies (Khalil, 2011). Once the drug and drug carrier have been radiolabeled with two distinct radioisotopes, it is possible to investigate, visualize and quantify their *in vivo* biodistribution and kinetics in parallel in a single animal. In preclinical studies, simultaneous dual-isotope imaging offers many advantages over separately acquired data such as reduction of the time for data acquisition and elimination of the experimental and physiological inter-animal variations (Hijnen et al., 2012; Tsuji et al., 1999). This technique has opened up new imaging possibilities to trace two compounds of interest such as a specific ligand and its nonspecific control ligand (Hijnen et al., 2012; Schmitt et al., 2008), a drug and its carrier (Sonaje et al., 2010), a drug and its analogue, antibody-drug conjugates (Ilovich et al., 2018) and important blood-proteins like albumin and transferrin (Smith et al., 1992).

SPECT radionuclides used for radiolabeling are typically metals or halogens emitting gamma energies between 30 and 300 keV, and half-lives varying between hours to several days. To date, pairs of radionuclides used in dual isotope imaging include ^{123}I/^{99m}Tc (Hsieh et al., 2010), ^{201}Tl/^{99m}Tc (Heo et al., 1994), ^{131}I/^{99m}Tc (Ceccarelli et al., 2004), ^{111}In/^{99m}Tc (Zhu et al., 2007), ^{111}In/^{67}Ga (Esquinas et al., 2018) and ^{111}In/^{177}Lu (Hijnen et al., 2012). The appropriate choice of the radionuclide allows tailoring the properties of the labeled compound to the application. For example, radiolabelling of peptides and antibodies require a radionuclide with relatively long half-life similar to their elimination half-life. Attaching metal radionuclides such as ^{99m}Tc, ^{111}In and ^{67}Ga to small molecules, peptides and proteins, e.g., antibodies, require the conjugation of DTPA, DOTA and NOTA, respectively. As these chelators are relatively large this ligand tethering/coordination could potentially change the biological activity of the altered compounds, especially for small molecule drug modification. To minimize the structural modification of radiolabeled compounds, radiohalogenation techniques are sometimes considered (Sugiura et al., 2014; Wilbur, 1992).

During radiohalogenation, the physicochemical and biological properties of the original molecule change only in a minor way, as typically (and ideally) either a hydrogen atom is replaced by a halogen, or a non-radioactive halogen is replaced with a radioactive halogen, such as ^{18}F for PET or ^{125}I for SPECT. The chemistry of incorporating radiohalogens into organic molecules has been well studied (Adam and Wilbur, 2005; Sutherland, 2019), with fluorine chemistry seeing new developments during the last few years (Liu et al., 2015; Pattison, 2019; Szpera et al., 2019; Uhrig et al., 2019). For the labeling of biopharmaceuticals, radioiodinations are simpler and thus preferred over other radiohalogens and allow to quantitatively study pharmacokinetics and biodistribution (Seevers and Counsell, 1982; Vaidyanathan and Zalutsky, 2019).

An efficient radioiodination method adds a radioactive iodine to a molecule without causing chemical and biological damage (Mock and Zheng, 2006). Examples for straight-forward iodinations are isotope exchange labeling, where a molecule with covalently bound stable iodine atoms on an aromatic ring is exchanged with a radioactive iodine atom, for example in the labeling of 2-[[3-(dimethylamino)propyl-methylamino]methyl]-4-(123I)iodanyl-6-methylphenol (^{123}I-HIPDM); a regional cerebral perfusion imaging agent (Lui et al., 1987). Peptides and proteins containing amino acids with aryl substituents, such as tyrosine residues (Schumacher and Tsomides, 2001) are good candidates for the addition of radioiodine after oxidation by chloramine-T (Lee et al., 1977), Iodobeads (Markwell, 1982) or Iodogen™ (Michael Conlon, 2002). Moreover, molecules such as fatty acids with carbon–carbon unsaturated bonds (commonly used in lipid based drug delivery systems), can be easily radioiodinated at the site of the double bond using either iodine monochloride or elemental radioiodine (Robinson and Lee, 1975).

Several isotopes of iodine emit gamma rays and can thus be used to detect biological, diagnostic, or pharmaceutical molecules in both

preclinical *in vitro* measurements and *in vivo* diagnostic imaging. The SPECT radioisotopes are ^{123}I, ^{125}I and ^{131}I, while a PET isotope (^{124}I) is also available (see **Table S1** in the supplementary material (NuDat)). Because of its high energy beta (up to 606 keV, 90.4%) and high-energy gamma (364 keV, 83%) emissions, ^{131}I is rarely used for imaging, as it delivers relatively high doses to tissues such as the thyroid and bladder, in addition to poor resolution in gamma camera images (Dewaraja et al., 2000).

^{123}I and ^{125}I have been widely used to study cellular dynamic biochemical processes, understanding drug metabolism and action, as well as establishing treatment strategies for these iodine isotopes individually (Bailey, 1994; Caplan and Baniyash, 2002). The main advantage for dual radiolabeling of organic compounds and simultaneous SPECT imaging with ^{123}I and ^{125}I is their identical chemical properties. A major problem from the physics imaging point of view, is that the energy of x-ray photons of ^{123}I overlap with the energy of the main gamma photons as well as the x-ray emissions of ^{125}I. Therefore, low-energy x-ray photons of ^{123}I are indistinguishable from ^{125}I emissions since the camera discriminates solely by energy (see Fig. 1). As a result, a naïve measurement of ^{125}I activity in the presence of ^{123}I using SPECT would result in an overestimation of the activity present in the imaging object. In order to get accurate measurements of activity distribution of ^{125}I in the context of ^{123}I/^{125}I dual isotope SPECT, it is necessary to develop a method to correct for the ^{123}I signal present in the ^{125}I photopeak (referred to as crosstalk).

To the best of our knowledge, the first attempt to address dual isotope imaging of ^{123}I and ^{125}I SPECT was presented by Lee S. *et al.* (Lee et al., 2015; Lee et al., 2013). In their study, the authors estimated the fraction of ^{123}I photons detected in the ^{125}I photopeak window by means of Monte-Carlo simulations of a mouse model under different experimental conditions. Although Monte-Carlo simulations would allow us to estimate correction factors for accurate activity quantification of ^{125}I in dual-isotope SPECT, such an approach is not very practical due to the complexity of Monte-Carlo methods to model the imaging system and experimental conditions.

More recently, a practical method to estimate and correct for the cross-talk signal of ^{123}I into the low-energy peak of ^{125}I was proposed by
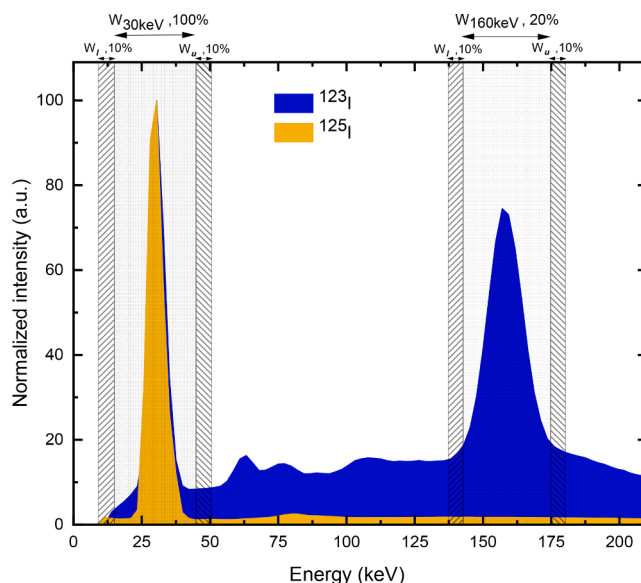
Fig. 1. Energy spectra of ^{123}I and ^{125}I acquired from the SPECT/PET/CT system equipped with NaI(Tl) crystals and UHR–RM collimator. Main photopeak windows (W_{160keV} and W_{30keV}) are reported in dot pattern. According to the background/scatter subtraction technique explained in Section 2.5, scatter windows (W_l: lower window, W_u: upper window) are shown in dense line pattern.

Tsartsalis *et al.* (Tsartsalis et al., 2018). In this work, the authors evaluated the feasibility of simultaneous ^{123}I/^{125}I SPECT imaging of the rat brain. However, the generalization of the proposed method into any animal/human imaging is not guaranteed since the authors were not able to perform corrections for photon attenuation or scatter, which limits the applicability of their method to just a set of imaging conditions identical to those used in their experiments.

In our study, we build on Tsartsalis's practical approach for ^{123}I/^{125}I imaging, sharing their philosophy, and address the major limitation of this prior work. We propose a simple and practical method to compensate for crosstalk in simultaneous ^{123}I/^{125}I SPECT imaging in a preclinical setting based on fully quantitative SPECT imaging. A preclinical imaging system was used to perform a series of phantom experiments under multiple imaging conditions in order to estimate the accuracy of the approach. Furthermore, to demonstrate the feasibility of the crosstalk compensation method in an *in vivo* setting, we investigated *in vivo* the passage of a lipid-based formulation (LBF) where a poorly water-soluble drug molecule was solubilized in a lipid excipient to enhance drug bioavailability. Fenofibrate was used as a highly lipophilic model drug (log P = 5.24) (Kevadiya et al., 2019; Kim et al., 2013) labeled with ^{123}I, and ^{125}I-labeled triolein, the largest component of Soybean Oil, was used as the exemplar lipid excipient and added to the formulation as a tracer. Understanding the interplay between hydrophobic drugs and their lipid excipients after administration might be helpful in choosing the best LBF with enhanced aqueous solubility (Tran et al., 2020).

2. Methods

A VECTor/CT scanner (MILabs, Utrecht, The Netherlands), a preclinical SPECT/PET/CT system equipped with NaI(Tl) crystals and ultra-high resolution (UHR–RM) collimator (1 mm pinhole size, sub-millimeter spatial resolution and > 700 cps/MBq sensitivity) was used in the present study. Na^{123}I was obtained from Nordion (Vancouver, BC, Canada) and Na^{125}I was obtained from American Radiolabeled Chemicals Inc. (St. Louis, MO, USA). A Biodex Atomlab 500 dose calibrator was used to measure activity for each experimental design. AMIDE, a Medical Image Data Examiner software (UCLA, CA, USA) was used for image registration, visualization and analysis (Loening and Gambhir, 2003). In this section, the crosstalk correction method for dual isotope ^{123}I/^{125}I SPECT is described (Section 2.1) and a series of phantom experiments performed to validate this approach (Section 2.2-2.4). Then, the image reconstruction and data correction techniques are applied to the SPECT data (Section 2.5). Finally, the *in vivo* experimental details are introduced (Section 2.6).

2.1. Crosstalk correction in dual isotope ^{123}I/^{125}I SPECT

The normalized energy spectra of two point-sources of ^{123}I and ^{125}I (obtained with VECTor, a small animal SPECT/PET/CT system equipped with NaI(Tl) crystals (Goorden et al., 2013) and ultra-high resolution (van der Have et al., 2009), referred to as UHR–RM, collimator) show two photopeak windows, one at higher energies (160 keV) and the other window far from the upper one in lower energy around 30 keV (Fig. 1). The high energy window (144–176 keV) contributes to ^{123}I gamma photons while 30 keV photopeak is the overlap of lower energy photons and x-rays of both ^{123}I and ^{125}I. To separate out the contribution of ^{123}I and ^{125}I in the overlapping area, a simple and straightforward method useful for preclinical SPECT imaging is introduced here.

In a ^{123}I/^{125}I SPECT acquisition, the total number of detected photons (i.e., counts) in the low energy photopeak window centered around 27–30 keV (the peak of X-Ray emissions of both ^{123}I and ^{125}I), C_{30}, is given by:

$$C_{30} = C_{30-^{123}I} + C_{30-^{125}I} + C_{scatter} \tag{1}$$

where $C_{30-^{123}I}$ correspond to the counts from photons emitted by ^{123}I (X-rays), $C_{30-^{125}I}$ correspond to the counts from photons emitted by ^{125}I (X-rays and gamma emission at 35 keV), and $C_{scatter}$ are scatter photons which could originate from both ^{125}I and ^{123}I emissions scattering within the object (e.g., a phantom or a small animal) and within the imaging system (e.g., collimator).

In our approach, the acquired photopeak counts C_{30} are first reconstructed with corrections for scatter and attenuation (see Section 2.5 for details on the image reconstruction and data correction methods). Subsequently, for activity quantification, a volume of interest (VOI) within the reconstructed image (e.g., the target organ in an animal study) is defined. The number of reconstructed counts R_{30} accumulated within this VOI are the sum of both counts from ^{123}I and ^{125}I emissions, under the assumption of accurate scatter correction:

$$R_{30} \approx R_{30-^{123}I} + R_{30-^{125}I} \tag{2}$$

The counts originating from the ^{123}I emissions in the low energy photopeak could be estimated indirectly from the reconstructed counts in the high-energy 160 keV photopeak as follows:

$$R_{30-^{123}I} \approx kR_{160-^{123}I} \tag{3}$$

where k is an experimentally determined conversion factor, which represents the ratio of counts between the 30 keV photopeak and the 160 keV photopeak of ^{123}I. In an ideal SPECT system (with perfect sensitivity and perfect energy resolution) with an image-reconstruction method with perfect scatter and attenuation corrections, this ratio should be equal to the ratio between the number of x-ray emissions and the number of 160 keV photons emitted per disintegration of ^{123}I. This factor was measured under real conditions with three simple phantom experiments (see Section 2.2).

Once the quantity $R_{30-123I}$ is known, the total reconstructed counts in the 30 keV photopeak which correspond to ^{125}I emissions can be determined as:

$$R_{30-^{125}I} \approx R_{30} - kR_{160-^{123}I} \tag{4}$$

Finally, the ^{125}I activity within the VOI is obtained by the product of the reconstructed counts $R_{30-125I}$ and the SPECT calibration factor for ^{125}I (CF$_{125I}$), which can be determined experimentally with a point-source scan (see Section 2.3 and 2.4). Fig. 2 summarizes the proposed crosstalk correction method.

2.2. Determination of the 30 keV to 160 keV ^{123}I photopeak conversion factor k

The conversion factor k was measured under different imaging configurations taking into account physical factors such as photon attenuation (Zaidi and Hasegawa, 2003) and scatter (Zaidi and Koral, 2004) encountered in imaging of small sized animals. The three reference conditions (RC$_1$, RC$_2$ and RC$_3$) consisted of a small vial filled with activity in air (point-like source; 0.2 mL, 100 MBq/mL), a small vial filled with activity placed in a large cylinder filled with non-radioactive water (which mimics focalized concentration of tracer within soft tissue in a small animal; 0.2 mL, 100 MBq/mL), and a large cylindrical syringe filled uniformly with activity (which represents an extended distribution of activity; 5 mL, 20 MBq/mL), respectively (**Table S2** in the supplementary material).

SPECT tomographic phantom images were reconstructed for high energy (144–176 keV) and low energy (15–45 keV) spectrums of ^{123}I and followed by scatter and attenuation correction. After segmentation of the same VOI in both high energy and low energy reconstructed images, the number of reconstructed counts for high and low energy photopeak windows were quantified by the mean activity value in the VOI as R_{160} and R_{30}, respectively. *Factor k* was determined from the ratio of R_{30} and R_{160}. The degree of variation of factor k was presented through coefficient of variation (CV%) calculation.
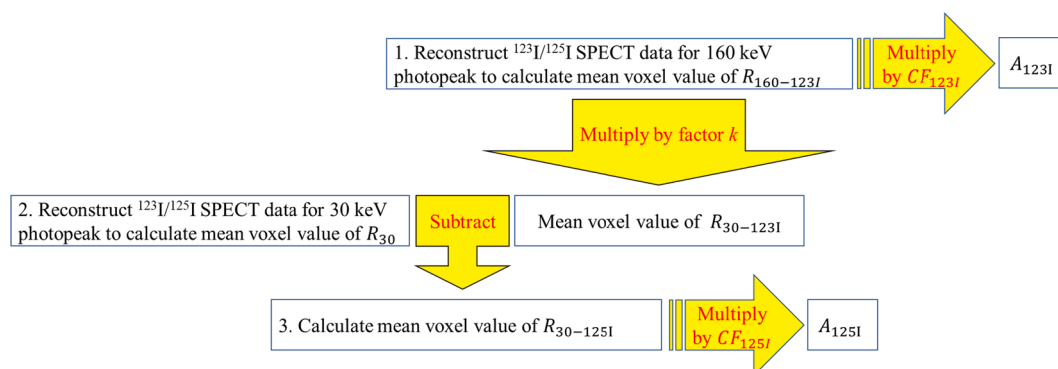
Fig. 2. Overview of the proposed crosstalk correction method in dual isotope $^{123}I/^{125}I$ SPECT. For more details on determination of CF_{123I} and CF_{125I} see section 2.3. A_{123I} and A_{125I} are activity concentrations for ^{123}I and ^{125}I, respectively.

2.3. Determination of ^{123}I and ^{125}I calibration factors for quantitative studies

For quantitative studies via tomographic imaging, the gamma camera calibration factor (CF) is a prerequisite to convert the activity count map to the absolute activity or activity concentration of the imaged object. For each specific isotope and imaging configuration (i.e., collimator and energy window settings), a new CF needs to be calculated. For each isotope at each RC, CFs were determined using the formula of **Eq. (5)**, where A is the activity of the source measured with a dose calibrator, V represents the voxel volume in the reconstructed image (in mL) and $\sum R_i$ represents the sum of voxel counts (arbitrary units) in a volume of interest (VOI) (Esquinas et al., 2017).

$$CF = \frac{A}{V \sum R_i} \tag{5}$$

In practice, CFs were measured by drawing a VOI around the activity in the point-like source (RC_1 and RC_2), while for the uniform syringe (RC_3), mean voxel values is measured in a uniform area in the middle of the phantom to avoid border effects. AMIDE was used to draw and analyze VOIs. Multiple RCs with known activity concentration were used. For ^{123}I isotope, the same activities and phantom geometries were used as in section 2.2 while the ^{125}I calibration measurements were done in configurations of RC_1 and RC_3 with 0.5 mL of a 37 MBq/mL activity concentration, and 20 mL of 2.37 MBq/mL activity concentration, respectively. Photopeak and scatter/background window settings used to create ^{125}I projections were similar to ^{123}I x-ray peak (15 – 45 keV). **Table S3** in the supplementary material summarizes energy window

setting for ^{123}I and ^{125}I used in CF_{123I} and CF_{125I} calculations, crosstalk correction and animal study.

2.4. Phantom study to assess accuracy of crosstalk correction method in $^{123}I/^{125}I$ preclinical SPECT

Phantom studies were used for two purposes. First, to measure the activity quantification accuracy of single ^{123}I and single ^{125}I SPECT in VECTor (i.e., to establish a baseline level of accuracy). Second, to determine the accuracy of the proposed dual-isotope method in $^{123}I/^{125}I$ dual isotope imaging (Section 2.1) and to understand its limitations. Experiments were designed to recover absolute activities both in single and dual isotopes imaging mode. For this purpose three simple multi-source phantoms (MSP) were made by placing 0.2 mL 6-strip Polymerase Chain Reaction (PCR) tubes (Fig. 3) inside a 20-mL plastic syringe filled with water. MSP1, MSP2 and MSP3 were filled with different activity concentrations (average volume 70 μL) of individual activities (^{123}I or ^{125}I) or mixtures thereof, and placed inside a 20-mL plastic syringe filled with water. **Table S4** in the supplementary material summarizes the range of activity concentrations used for this validation study.

Validation of single $^{123}I/^{125}I$ quantitative SPECT: SPECT images of phantoms MSP1 and MSP2 were acquired followed by a CT scan for attenuation correction, reconstructed and corrected using the same settings as those used in calibration. Small spherical VOIs inside the vials (V = 27.8 mm³) were manually drawn, and the average counts/voxel calculated using AMIDE. Then, CFs (obtained from different RCs) were used to convert the average counts/voxel for each phantom to their
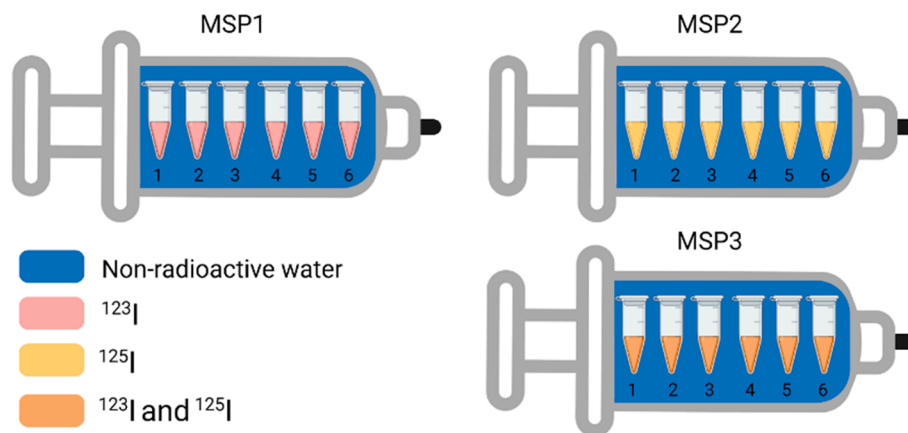
Fig. 3. Phantom used for activity quantification measurements of single and dual isotopes. First, 6 PCR tubes filled with various ^{123}I activity concentrations (MSP1), various ^{125}I activity concentrations (MSP2) and finally with $^{123}I/^{125}I$ mixtures at various ratios (MSP3). PCR tubes filled with radioactivity were placed inside a 20 mL syringe filled with non-radioactive water. Created with BioRender.com.

corresponding activity concentrations. The difference between the known activity concentration (referred to as true value, measured with dose-calibrator) and SPECT activity concentration (measured value) was calculated for each individual vial within each phantom (MSP1 and MSP2). The difference is presented as (+/-) percentage of the true value.

Validation crosstalk correction technique: The accuracy of crosstalk correction was evaluated as a function of the ^{123}I to ^{125}I concentration ratio. The MSP3 phantom contained mixtures of ^{123}I/^{125}I radionuclides at 6 different ratios (approximately A_{123I}:A_{125I} of 3:1, 2:1, 1:1, 1:2, 1:7 and 1:14) (**Table S4** in the supplementary material). To recover the activity concentration corresponding to each isotope, the technique introduced in Section 2.1 was used. SPECT images of phantoms MSP3 were reconstructed separately for 30 and 160 keV photopeaks windows and corrected for scatter and attenuation. After measuring the average count-rate on the VOI drawn inside the vials reconstructed for the 160 keV photopeak window $(R_{160-123I})$ and multiplying by the factor k obtained from RC_2, ^{123}I low energy x-ray emissions $(R_{30-123I})$ were estimated. Then, $R_{30-123I}$ was subtracted from the average count-rate on the same VOI in the image reconstructed for 30 keV photopeak window (R_{30}) to identify the contribution of ^{125}I $(R_{30-125I})$ to the total reconstructed counts in the low energy peak. The difference between the known activity concentration of each isotope in the mixture (true value) and their measured crosstalk corrected SPECT activity concentration was calculated. The difference is presented as (+/-) percentage of the theoretical value.

2.5. Image reconstruction and activity quantification

All SPECT images were acquired in list-mode and following each SPECT acquisition a CT scan using a tube setting of 60 kV and 615 µA was obtained. To generate SPECT images, the recorded counts in list-mode were decay corrected and binned corresponding to the main photopeaks of ^{123}I and ^{125}I, 160 keV (20% width) and 30 keV (100% width), respectively. SPECT images were reconstructed using a pixel-ordered subset expectation maximization (POSEM) algorithm (Branderhorst et al., 2010) using 16 subsets, 10 iterations and an isotropic 0.4 mm voxel grid with U-SPECT Rec2.5li software (MILabs). The CT projection data was reconstructed using SkyScan NRecon software (Microphotonics, Allentown, PA, USA) to generate a 3D image with a 0.169 mm^3 voxel size. To correct for self-, high-energy and background scatter within the photopeak window, triple energy window (TEW) methods were used during the iterative reconstruction (Ogawa et al., 1991). Two adjacent narrow sub-windows (10% width) were set on each side of the photopeak. Reconstructed images were post-filtered with 1 mm FWHM Gaussian kernel to minimize the effect of noise.
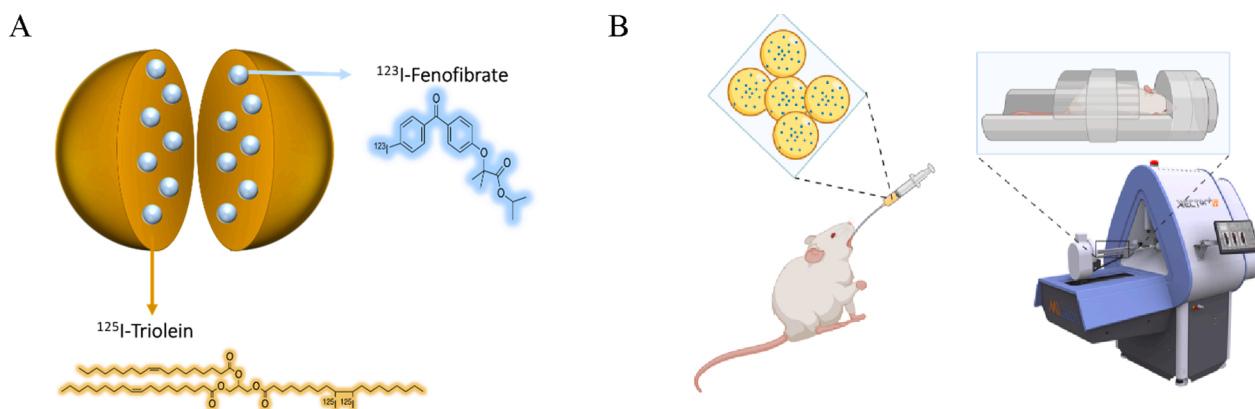
2.6. Animal study

The LBF was prepared with radioactive ^{123}I-Fenofibrate as the lipophilic model drug and ^{125}I-labeled triolein in soybean oil as the excipient (or drug delivery system), as shown in Fig. 4 and described in more detail previously (Tran et al., 2020). An imaging study was performed in three male Sprague-Dawley rats (Charles River, Canada) weighing 335 $\pm$ 18 g (average $\pm$ SD) in accordance with the Animal Care Committee of the University of British Columbia under the approved protocol A16-0150. The sex and age of the animals was kept the same as the earlier performed traditional pharmacokinetic rat study to which all results were compared (Tran et al., 2020). The group size was 3, instead of 5 in the traditional study, to allow for the chosen imaging time points. Rats were gavaged with 0.4 $\pm$ 0.02 mL of LBF containing ^{123}I-Fenofibrate (28.19 $\pm$ 2.06 MBq) and ^{125}I-Triolein (8.14 $\pm$ 0.4 MBq). Under isoflurane anaesthesia (5% for induction, 1–3% during scanning), the animals were imaged 30 min, 5, 9.5 and 24 h later by SPECT including a CT scan for anatomical information and photon attenuation correction to obtain fully quantitative images.

To obtain the pharmacokinetic profiles of ^{123}I-Fenofibrate and ^{125}I-Triolein, AMIDE software was used to to generate 3D maximum intensity projection (MIP) renderings and draw spherical VOIs (3 mm in diameter) inside organs of interest using the registered CT images to determine the time activity pattern per target organ. The delineated organs were stomach, intestine, heart and liver.

^{123}I activity distribution was determined in the reconstructed images from the 160 keV photopeak window. To estimate ^{125}I activity distribution, factor k obtained from RC_3 was used to correct for the cross-counts in the lower energy window, as described in Section 2.4. Finally, the ^{123}I and ^{125}I mean activity in each VOI (counts/pixel) were multiplied by their corresponding CFs (obtained from RC_3) to calculate the activity concentration in each organ (MBq/mL). Results were expressed as standardized uptake values (SUVmean, **Eq. (6)**) by normalizing the organ concentrations with the individual animal's body weight and administered dose according to the following equation:

$$SUV\ [g/mL] = \frac{Concentration\ in\ volume\ of\ interest\ [MBq/mL]}{Injected\ dose\ [MBq]}$$
$$\times Body\ weight\ [g] \tag{6}$$

All SPECT images were decay-corrected to the time of administration. Rats were euthanized for *ex vivo* quantification of the biodistribution after the final imaging time point, and the radioactivity in the organs was determined by γ-counting. Selected organs were removed and transferred into a pre-weighed counting tube. The amount of ^{123}I and ^{125}l in each sample was measured simultaneously using 130–190 keV and 15–75 keV windows, respectively, in a calibrated

Fig. 4. Schematics of (A) lipid-based formulation (LBF) prepared with radioactive ^{123}I-Fenofibrate as the lipophilic model drug and ^{125}I-labeled triolein in soybean oil as the excipient. (B) Rats are gavaged with the lipid formulation, followed by simultaneous dual-isotope SPECT imaging with the VECTor imager at 30 min, 5 h, 9.5 h, and 24 h thereafter. Created with BioRender.com.

gamma counter (Packard Cobra II 5010 Auto-gamma counter, Perkin Elmer, Waltham, MA, USA). Standard sources of ^{123}I and ^{125}I isotopes with known activities were used to find the crosstalk correction factor between both isotopes in the 15–75 keV window to determine the correct ^{125}I counts.

Pharmacokinetic parameters for both the traditional and the SPECT-based studies were estimated based on a 1-compartment model (i.e., central compartment) with first-order absorption and linear clearance using NONMEM v7.4.1 (ICON Plc, Dublin, Ireland). Models were fit using a naïve pooled approach based on non-linear minimization of a maximum likelihood error function. One data point from the ^{123}I-Fenofibrate SPECT imaging was censored in the analysis due to the presence of a relatively high initial concentration during the absorption phase that was discordant from observed values in other preclinical specimens.

To compare the results from the radioactive imaging studies to the previously performed traditional PK study of ^{3}H-labeled fenofibrate in rats (Tran et al., 2020), the plasma concentrations (μg/mL) were transformed into SUVs (g/mL) according to the following formula:

$$SUV \ [g/mL] = \frac{Plasma \ concentration \ [\mu g/mL]}{Injected \ dose \ [\mu g]} \times Body \ weight \ [g] \qquad (7)$$

To account for differential partitioning of fenofibrate in plasma versus whole blood, the latter of which represents the analyzed matrix in SPECT imaging studies, plasma derived SUVs were multiplied by a factor of (1 – hematocrit). A hematocrit of 0.3961 was used for all calculations (Probst et al., 2006). The denoted conversion assumes fenofibrate partitioning into red-blood cells is limited owing to its high degree (>99%) of plasma protein binding (Chapman, 1987; Desager et al., 1982).

3. Results and discussion

Tracing two radiopharmaceuticals quantitatively *in vivo* by SPECT imaging requires that the gamma-emitting radioisotopes have distinct energy emission spectra, so that both can be accurately identified over time. For the two radioisotopes ^{123}I and ^{125}I with overlapping energy spectra at lower energies, dual SPECT imaging is not straightforward. Here we present a simple method for dual isotope SPECT quantification for mixtures of ^{123}I and ^{125}I that can be used with any preclinical SPECT imager and would, as shown here, be especially advantageous for the investigation of the fate of small drugs and their drug delivery system.

3.1. Crosstalk correction in dual isotope ^{123}I/^{125}I SPECT

The present crosstalk correction method mainly relies on quantitative reconstruction of SPECT data as well as scatter and attenuation corrections to calculate the 30 keV to 160 keV ^{123}I photopeak conversion factor k and distinguish the contribution of each isotope in the overlapping peaks of the lower energy spectra. To investigate how factor k changes as a result of variabilities in scatter and attenuation, various phantom configurations were applied. They consisted of a small plastic vial filled with activity placed in air (RC$_1$) or inside a large cylinder filled with non-radioactive water (RC$_2$). Mimicking the pre-clinical conditions encountered in animal studies, a large cylinder with no inserts was used, uniformly filled with activity (RC$_3$) to assess the practicality of the scanner to image an extended volume source.

Table 1
Crosstalk correction factors k determined in the different phantom setups.

	k factor
RC$_1$	0.721
RC$_2$	0.735
RC$_3$	0.850
CV%	9.1%

The differences in k factors of the different phantom geometries were minor (Table 1). For example, it was $k = 0.721$ for RC$_1$, with almost no scatter and attenuation, compared to the point source RC$_2$ which was $k = 0.735$ located inside a syringe filled with water as the attenuating media. For an extended volume source where a plastic syringe was filled homogenously with ^{123}I, a slightly higher ratio ($k = 0.850$) was measured as the result of scattering of higher energy photons which ended up in higher counts in the lower energy window (Table 1). The coefficient of variation of less than 10% in k values shows the applicability of the utilized SPECT imager in correction for scatter and attenuation and confirms it as a feasible technique to correct for overlapping spectra in ^{123}I/^{125}I dual isotope preclinical studies.

It is worth comparing our experimental determination of k with that of Tsartsalis et al., 2018 (referred to as α factor in their manuscript). In this prior work, the authors measured a k factor equal to 0.58 using phantom experiments, while it was approximately equal to 0.34 in *in vivo* measurements of a rat brain. The lower value obtained in Tsartsalis's phantom experiment compared to ours could be explained by the fact that their proposed method did not utilize corrections for attenuation (nor scatter). In such a scenario, photons emitted at approximately 30 keV from ^{123}I will be attenuated much more than those emitted at 160 keV, resulting in an under-estimation of the low-energy peak signal compared to our approach, which takes photon attenuation into account. Their scenario might also explain why the authors measured a much smaller factor in the *in vivo* study, where attenuation of low-energy photons is expected to be greater than in the phantom.

3.2. Determination of ^{123}I and ^{125}I calibration factors for quantitative studies

To determine scanner calibration factors for each specific isotope, various imaging conditions were evaluated (RC$_1$, RC$_2$ and RC$_3$). SPECT data were reconstructed for main photopeaks of ^{123}I (160 keV) and single photopeak of ^{125}I (30 keV), respectively. The reconstructed images were attenuation/scatter corrected to compensate for these degrading physical effects. In total, 5 calibration factors were determined (for 2 radioisotopes and 3 reference configurations) and their values are reported in Table 2. Because the probability of scattering inside the point source is quite small, CF obtained from point source in air (RC$_1$) was considered to be the most accurate CF value. CFs obtained from RC$_2$ and RC$_3$ for ^{123}I and ^{125}I agreed within 4.1% and 0.3% of the reference CF value, respectively.

3.3. Phantom experiments

Validation of single ^{123}I/^{125}I quantitative SPECT: To compare the performance and accuracy of our SPECT/CT preclinical imager in translating reconstructed and corrected count maps of ^{123}I and ^{125}I isotopes into absolute activity and activity concentration maps, SPECT/CT images of phantoms MSP1 and MSP2 with known activity concentrations were acquired, reconstructed and corrected. Fig. 5 illustrates the comparisons of the measured activity concentration values obtained by each calibration factor for isotopes of ^{123}I and ^{125}I, respectively.

The three CF$_{160(keV)}$ calibration factors (determined from RC$_1$, RC$_2$ and RC$_3$) could recover the activity concentration of ^{123}I in MSP1 geometry within a range of −15.5% to −3.3% of their true value. The largest difference from the phantom values was −15.5% for 100.83

Table 2
CFs obtained from phantom studies using different reference configurations.

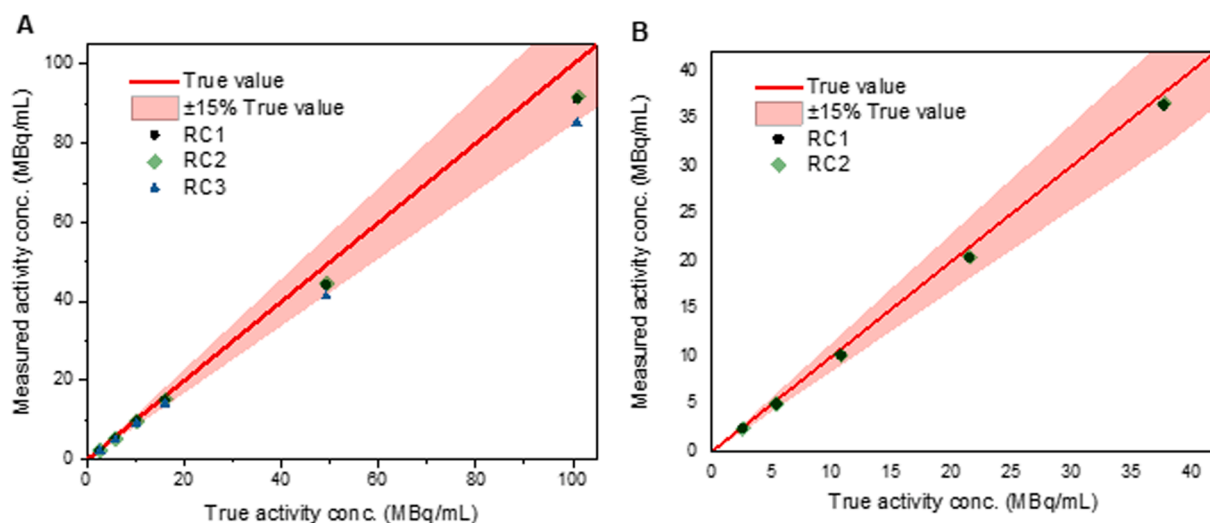|	^{123}I	^{125}I
	CF$_{160(keV)}$ (MBq/mL)	CF$_{30(keV)}$ (MBq/mL)
RC$_1$	688.4	516.7
RC$_2$	691.9	NA
RC$_3$	642.4	518.8

Fig. 5. Impact of different calibration factors in recovering activity concentration. (A) Validation of $CF_{160(keV)}$ for ^{123}I and (B) validation of $CF_{30(keV)}$ for ^{125}I. Expected activity concentration values (true value) are shown as a red line $\pm$ 15% area of true values.
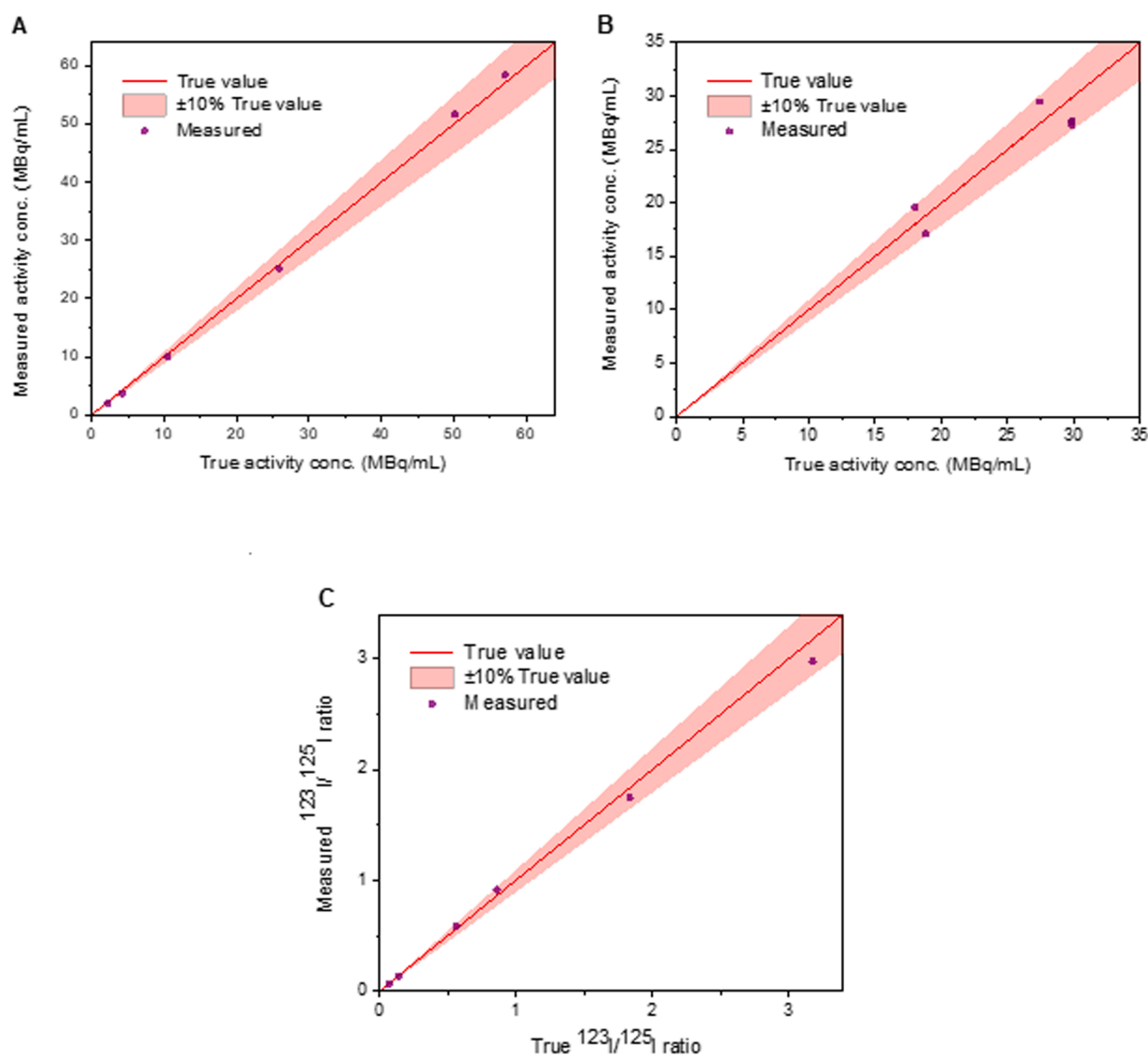

Fig. 6. $^{123}I/^{125}I$ dual-isotope validation. Comparison of the measured activity concentration values of (A) ^{123}I, and (B) ^{125}I in mixtures of $^{123}I/^{125}I$ and (C) $^{123}I/^{125}I$ activity ratio versus their expected (true) values shown as a red line $\pm$ 10% area of true values.

MBq/mL recovered by $CF_{160(keV)}$ obtained from RC_3. Data are summarized in the supplementary Tables S5 and S6.

Validation crosstalk correction technique: The MSP3 phantom was used to test and validate the crosstalk correction technique in differentiating the activities belonging to each isotope. Six combinations of known activity concentration of ^{123}I and ^{125}I were used with approximate activity ratios (A_{123I}:A_{125I}) of 3:1, 2:1, 1:1, 1:2, 1:7 and 1:14. The activity concentration was recovered for each isotope of each mixture and later was compared to their true activity concentrations. The crosstalk correction technique provided recovery of activity concentrations for ^{123}I in the mixture as well similar to those obtained in the single ^{123}I SPECT experiment. In all cases, ^{123}I activity concentrations in mixtures of ^{123}I/^{125}I were measured within ± 10% of the expected value (Fig. 6**A and 6B**). Furthermore, recovered ^{123}I to ^{125}I activity ratios were within ± 7% of the actual concentration ratios (Fig. 6**C**). The result of the experimental measurements is shown in **Table S7** in the supplementary material.

3.4. In vivo study

The dual-isotope protocol was tested in an *in vivo* experiment by studying the biodistribution and bioavailability of the poorly water-soluble drug fenofibrate delivered in a lipid-based formulation (LBF). For the study, three rats were administered by oral gavage with the LBF consisting of the ^{123}I-labeled highly lipophilic model drug ^{123}I-Fenofibrate (Kevadiya et al., 2019; Kim et al., 2013) in a lipid soy bean oil base that contained also the ^{125}I-labeled excipient triolein, which is one of the lipid components of the oil. To study the oral bioavailability of both the drug and the excipient with quantitative ^{123}I/^{125}I SPECT imaging, the technique described in Section 2.1 for the phantom studies was used. To separate the activity distribution of ^{123}I and ^{125}I from simultaneously acquired data, the contribution of ^{123}I to the ^{125}I emission window was calculated and subtracted within AMIDE, as explained in Fig. 2.

A representative rat from this experiment and the temporal behaviors of the two radiotracers and their characteristic movements through the gastrointestinal tract and through other organs over 24 h after oral gavage are shown in Fig. 7. The dual-labeled LBF was directly deposited into the stomach as a homogenous mixture. The reconstructed activity was digitally colored blue for ^{123}I and yellow for ^{125}I, resulting in an overall green color. While most of the mixture is still in the stomach after half an hour, a small amount has entered the small intestine, still homogenously mixed, as shown by the green color. Five hours later, there is still a significant green amount of LBF in the stomach which points to a homogeneous LBF mix. Further down the gastrointestinal tract, most of the lipid (in yellow) has now been absorbed, while some of the fenofibrate (in blue) is moving deeper into the intestinal tract. Fenofibrate thus seems to be absorbed significantly slower than the oil base.

At the next time point at 9.5 h, there is still a significant amount of homogenous drug/lipid mix in the stomach (in green), in a "stuck" position. Some of the ^{125}I-triolein is leaving the stomach, while it becomes even clearer that further into the intestinal tract, only fenofibrate is still present and waiting to be absorbed (or excreted). Once the triolein has been absorbed, some of it is metabolized. During this process, radioactive iodine is released into the blood stream in the form of free ^{125}I, which is immediately extracted with high efficiency by the thyroid. This is clearly visible at the 5 and 9.5 h time points as a strongly colored yellow thyroid. Only at the 24 h time point, however, can some ^{123}I uptake be clearly seen in the thyroid that comes from the fenofibrate radiolabel. Together with the already present ^{125}I, the color of the thyroid now appears green.

The SPECT dual imaging clearly shows a high concentration of a homogenous drug and lipid mix in the stomach, even 24 h after oral gavage. No activity is visible in the intestines at that time point. This was a very curious and unexpected result. Only after sacrificing the animals and analyzing the stomach content did we find out that the LBF was mixed together with sawdust and clumped into a ball. Rats are coprophagous and eat their feces and bedding materials, which in this case was fine wooden shavings, especially when they are hungry. In our experiment, the rats were fasted overnight, as a non-empty stomach influences the uptake of fenofibrate. However, similar experiments should in the future be done with no edible bedding material present in the cages. Further feeding optimizations, for example the use of liquid diets, could be investigated according to Jeffrey *et al.* (Jeffrey et al., 1987).

The volume of interest (VOI) analysis of the different organs confirmed the optical SPECT/CT description of the uptake and distribution of the drug and the lipid excipient in a quantitative way (Fig. 8).
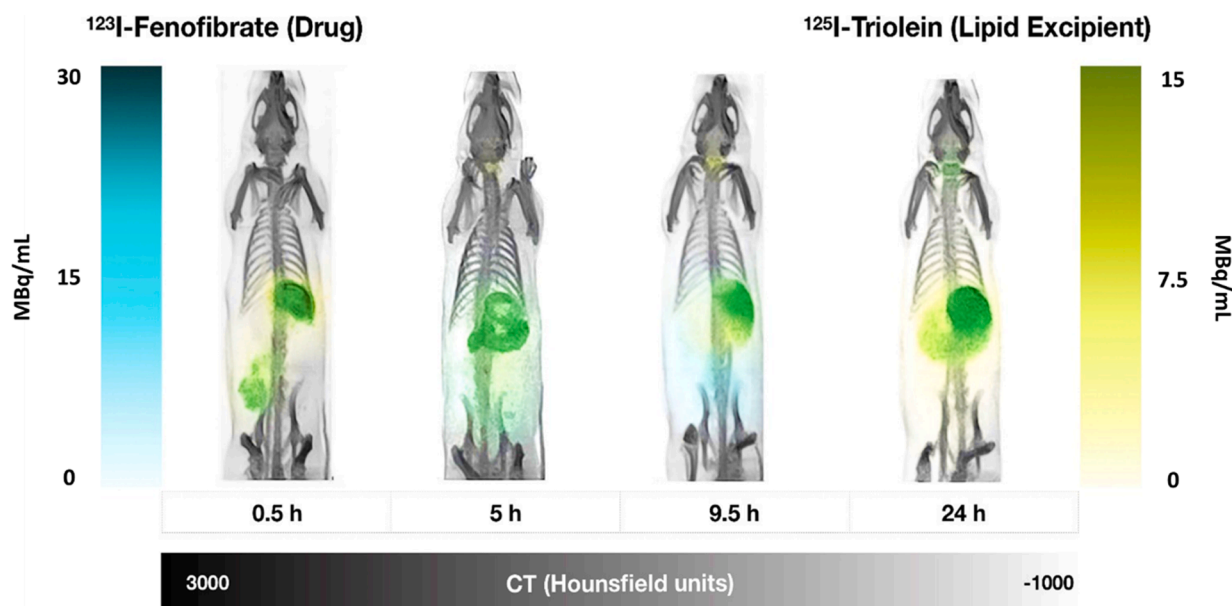
Fig. 7. Three-dimensional (3D) volume-rendered SPECT/CT images of radiolabeled drug (in blue) and radiolabeled lipids (in yellow) distributed in rats at 30 min, 5 h, 9.5 h, and 24 h after oral administration of the ^{125}I-triolein spiked soybean oil mixed in with the drug ^{123}I-Fenofibrate. Regions where both radiolabels overlap appear green.
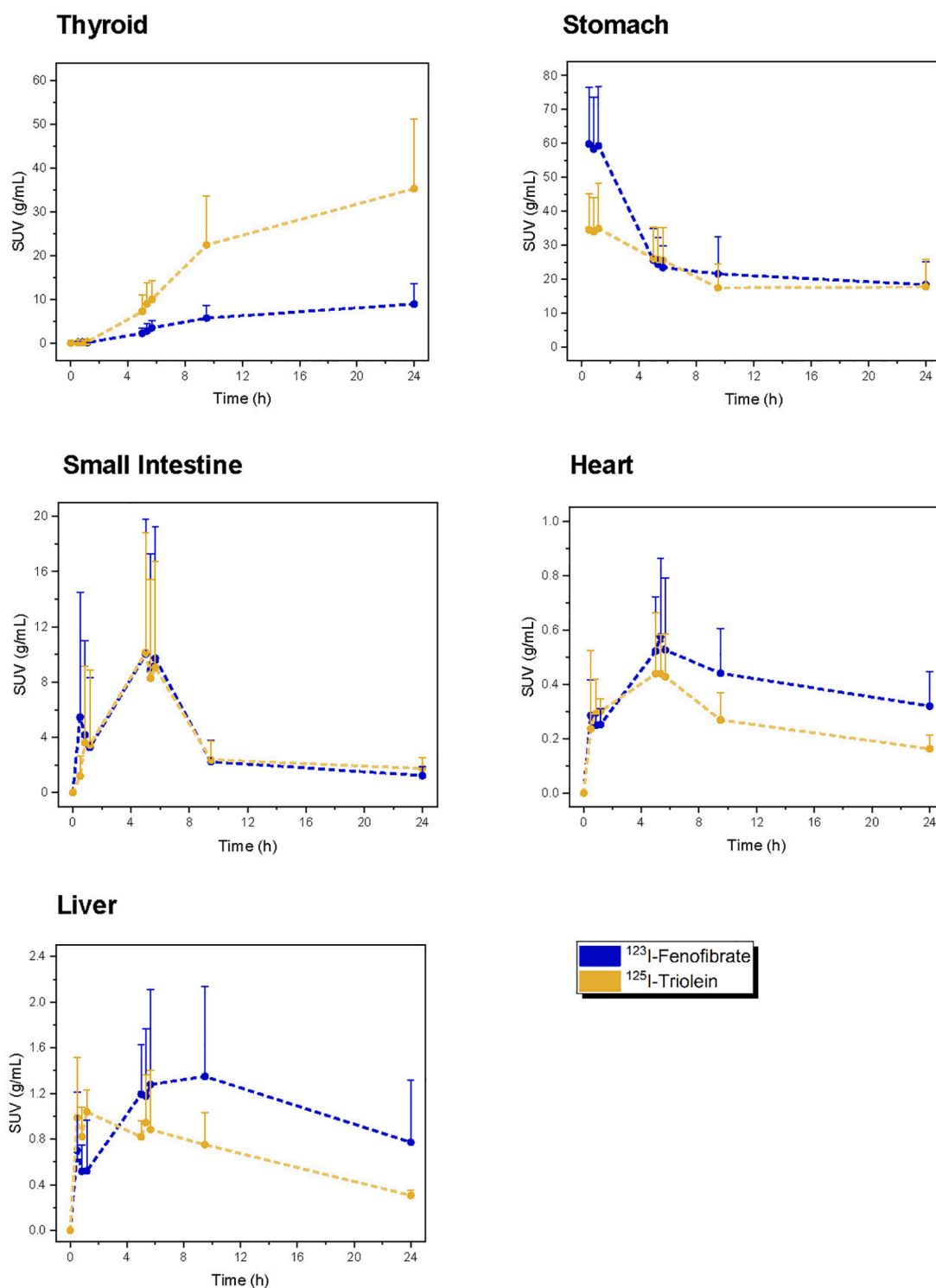
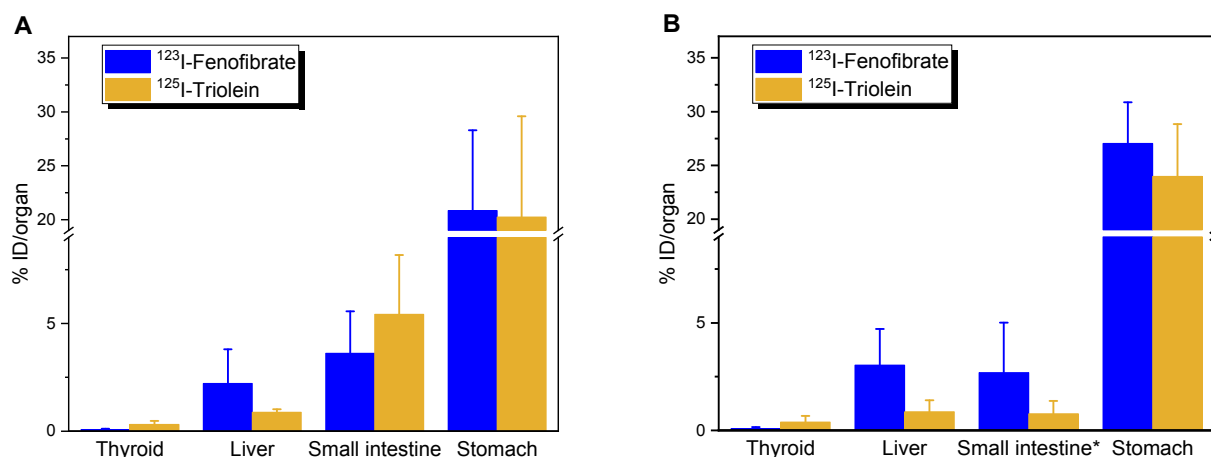**Fig. 8.** Standardized uptake value (SUV) of ^{123}I-Fenofibrate (radiolabeled drug, blue) and ^{125}I-Triolein (radiolabeled lipid excipient, orange) over 24 h after oral administration in rats in thyroid, stomach, small intestine, heart, and liver based on SPECT/CT images. Data are presented as mean + SD (N = 3).

In the stomach, both radioisotopes showed a similarly rapid clearance rate during the first 5 h which slowed down considerably from 9.5 − 24 h post administration. In all organs, the radiolabeled lipid appeared significantly faster and at higher concentrations (p less than 0.001) than the radiolabeled drug (Fig. 8).

According to Fig. 9, there was a good correlation between the data from the SPECT images and the ex vivo data, indicating that crosstalk compensation can provide substantial correction in distinguishing isotopes in simultaneously acquired data. The only organ that did not agree well was the small intestine, which was likely due to different sampling. In the SPECT analysis, we are forced to analyze the intestine including its content, due to resolution limitations, while the bio-distribution study can cleanly separate the activity in the intestinal wall from the content activity. Unfortunately, we did not separately analyze the contents, which should be done in the future.

Fig. 9. Organ distribution of ^{123}I-fenofibrate (radiolabeled drug) and ^{125}I-triolein (radiolabeled lipid excipient) (A) based on SPECT/CT image analysis at 24 h and (B) measured in the gamma counter at 25 h after oral administration. Data is expressed as a percentage of the injected dose per organ and presented as the mean $\pm$ SD (N = 3). *Explained in detail in the text.

3.5. Comparison of in vivo SPECT imaging to traditional PK study

To understand the true value of a new or not commonly applied method, it is important to compare it to the current gold standard and discuss advantages, limitations and points that might not be important in the traditional method. In this part, we are trying therefore to compare the pharmacokinetics derived from SPECT imaging with the classic drug sampling method in plasma. Both data sets were analyzed using a 1-compartment model with first-order absorption and linear clearance.

A first step before comparing traditional *vs.* SPECT PK is to make sure that the same organs/tissues are looked at, converted to congruent units, while also considering the sampling matrix as exactly as possible. For example, to directly compare the traditional fenofibrate plasma concentrations in µg/mL (Fig. 10A) to the most often used standardized uptake values (SUVs) in nuclear imaging, we first had to estimate the drug concentration in whole blood using an organism specific hematocrit value. Further, it had to be verified that the drug would not partition into the red blood cells (or consider what percentage would do that), as the degree of drug partitioning into the red blood cells would influence computed blood-specific PK parameter estimates. Thereafter, it was possible to convert the drug concentrations of the non-radioactive drug directly into SUVs with the help of equation (7) (Fig. 10B). As expected,

the converted SUV-time profile produced identical estimates for T_{max}, absorption half-life and elimination half-life compared to the traditional PK analysis (Table 3). Due to the change in concentration unit, the absolute values of AUC, C_{max}, clearance and volume of distribution, however, are different.

After converting traditional PK parameters to SUV-based parameters, a comparison of the plasma study to the SPECT imaging study was directly possible, see columns 3 and 4 in Table 3. While the absorption half-life and the T_{max} were similar, the elimination half-lives were discordant. The estimated elimination half-life from the SPECT imaging study was ~ 3.8x longer compared to the traditional PK study. In contrast, estimated apparent clearance values were similar between the two studies. Apparent clearance represents the proportionality constant relating administered dose to drug exposure. As such, following application of similar dosages, congruent exposure values (AUC_{0-inf}) were observed in the SPECT imaging and traditional PK studies. An explanation for the noted disparity in PK parameters between studies might be that measuring plasma concentrations is a very exact science, within a few percent, while the imaging of the moving heart, with its largest concentration of blood in the body, as a stand-in for blood concentrations suffers from resolution limitations, movement artefacts that for example lower the actual concentration due to having heart muscle tissue in the analysis window for part of the analysis time. Overall, this
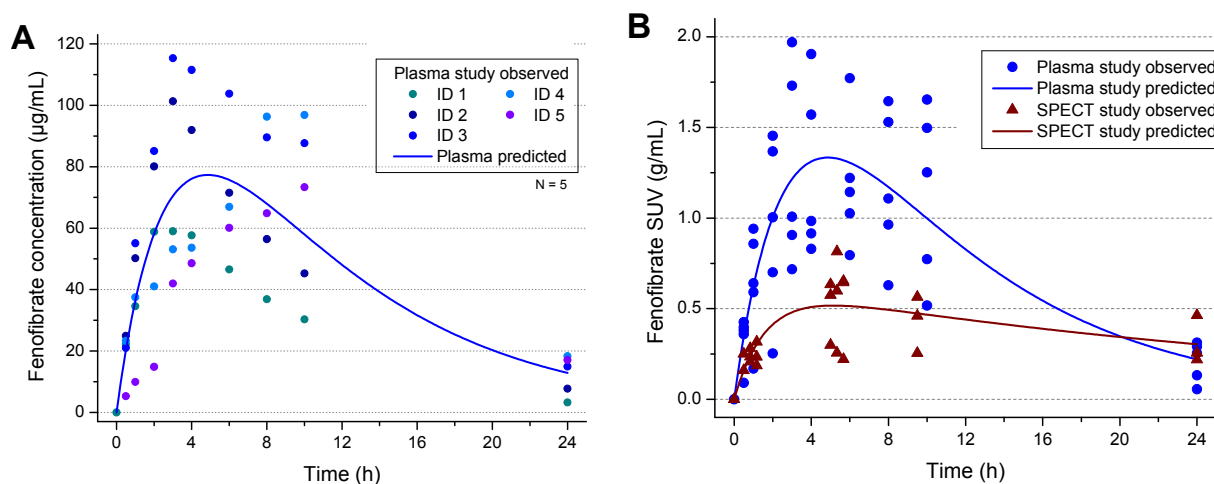
Fig. 10. Comparison of observed data to model predictions for the (A) plasma pharmacokinetic (PK) study, and (B) the SPECT imaging study. In addition, subplot B includes a comparison to SUVs derived from the plasma PK study.

reduced the apparent fenofibrate concentration measured by SPECT by a factor of 2.5.

Using the imaging-based method, we were additionally able to determine the PK parameters of one of the carrier matrix components, ^{125}I-Triolein. Doing that in the same animals that were used to determine the drug ^{123}I-Fenofibrate PK, at the same time, is beneficial and immediately gives a visual expression of where the two components reside at different time points. What for example became immediately clear is that a large proportion of the gavaged drug and drug carrier were unabsorbed from the gastrointestinal tract. This was not clear from the initial conventional PK data, where only plasma concentration–time data was available following administration of drug via an oral gavage (Tran et al., 2020). Of note, such study designs lack a capacity to inform if the extent of gastrointestinal absorption is complete. Doing a pilot imaging study in just a few animals, maybe even just one animal, would immediately have pinpointed that the formulation became trapped in the stomach, something that might not happen in other animal species or later in humans.

A direct comparison of the SPECT imaging data of drug and carrier shows that the lipid carrier reaches the blood compartment faster and is also cleared from blood faster (Fig. 11). The PK analysis confirms these findings (Table 3) with an absorption half-life of 1.31 h *vs.* 0.31 h and an elimination half-life of 22.41 h *vs.* 14.57 h for ^{123}I-Fenofibrate *vs.* ^{125}I-Triolein, respectively.

There are several limitations to our study. First, it was not ideal that the traditional PK study was done at a separate time and in a different lab than the imaging study. A second limitation was that the bioavailability determinations were compromised by the binding of the formulation to saw dust in the rats' stomach. This, however, was an important finding, which would have been missed without SPECT imaging, and which will make us alter future studies. A third limitation has to do with the fact that it might be easier to apply the system in less challenging systems than the oral gavage one in this study. For example, analyzing an intravenously injected drug delivery system ideally in a situation where the drug concentrations are at the same time measured in plasma or in whole blood samples from the same animals that are being imaged might yield closer agreement of the data.

Finally, another general limitation of radioactive SPECT imaging is that the stability of the imaging agent in biological fluids needs to be known before starting the study. Even before synthesizing a compound it is possible to determine if radioiodination of a compound is viable based on some general radioiodine stability principles. Cavina et al. have published an excellent article where it becomes apparent what compounds might be useful for imaging with radioactive iodine, and which ones are not (Cavina et al., 2017). Unfortunately, SPECT images do not
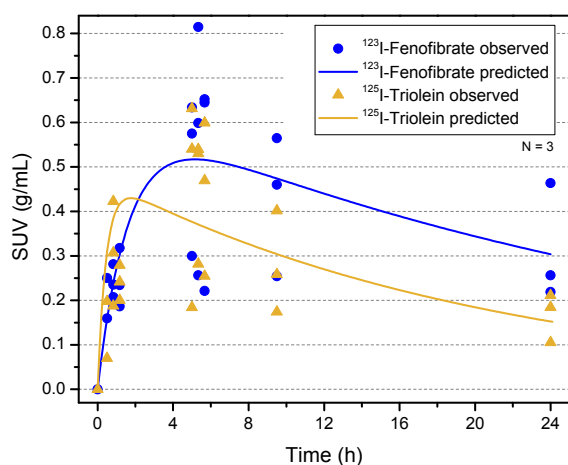
Table 3

PK parameters of the drug fenofibrate and the lipid excipient triolein in soy bean oil following oral administration. The data are presented as the mean.

Pharmacokinetic Parameter	Fenofibrate Plasma Sampling	Fenofibrate Plasma Sampling SUV	^{123}I-Fenofibrate SPECT Imaging SUV	^{125}I-Triolein SPECT Imaging SUV
	[N = 5]	[N = 5]	[N = 3]	[N = 3]
$T_{1/2}$ absorption (h)	2.08	2.08	1.13	0.31
CL/F (mL/h)	10.00	16.6	17.1	34.1
V_d/F (mL)	86.40	143	553	717
$T_{1/2}$ elimination (h)	5.99	5.99	22.41	14.57
T_{max} (h)	4.87	4.87	5.14	1.77
$C_{max,plasma}$ (µg/mL)	77.33	-	-	-
$C_{max,SUV}$ (g/mL)	-	1.33	0.52	0.43
$AUC_{0-24h,plasma}$ (µg × h/mL)	1061.61	-	-	-
$AUC_{0-24h,SUV}$ (g × h/mL)	-	18.28	9.77	6.62
$AUC_{0-inf,plasma}$ (µg × h/mL)	1173.20	-	-	-
$AUC_{0-inf,SUV}$ (g × h/mL)		20.19	19.60	9.83

SUV, Standardized uptake value; C_{max}, model predicted plasma maximum concentration or SUV; T_{max}, model predicted time of plasma maximum concentration or SUV; $T_{1/2}$, model-estimated half-life; AUC_{0-24h}, model predicted area under the concentration–time or SUV-time curve between 0 (time of dose administration) and 24 h; AUC_{0-inf}, model predicted area under the concentration–time or SUV-time curve between 0 (time of dose administration) and infinity; V_d/F, model predicted apparent volume of distribution; and CL/F, model predicted apparent clearance.

tell if we are imaging the original radiolabeled drug, a metabolite, or the radioisotope that has been released from the radiopharmaceutical. In our study, the release of the radioactive iodine from the drug or lipid is clearly visible, as its high affinity to the thyroid makes it show up there once released. Both fenofibrate and triolein are not known to accumulate in the thyroid, and activity in that organ thus does not represent their true biodistribution. In general, the appearance of a radioactive metabolite will result often in a prolonged half-life.

4. Conclusion

Herein, a practical method to perform quantitative ^{123}I/^{125}I dual-isotope SPECT imaging for pre-clinical imaging research was proposed and validated. Because of the low energy windows used, a low-energy collimator is optimal for good image quality and quantitative analyses. As the low-energy gamma energy of ^{125}I is at the same location as the main x-ray energies of ^{123}I, it is necessary to first determine the activity of the ^{123}I with the help of its 160 keV peak, then calculate the activity under the low-energy peak by multiplying its activity with the calibration factor for ^{123}I, and then finally subtract the found counts from the measured low energy counts, which after multiplying with the ^{125}I calibration factor, yields the true activity of ^{125}I in the mix. Our phantom studies demonstrated that activity quantification errors below 15% were obtained with mixtures of ^{123}I:^{125}I from 1:20 to 20:1.

The feasibility of quantitative ^{123}I/^{125}I dual-isotope SPECT imaging was then demonstrated in an animal study that described the fate of the drug fenofibrate after oral application. It could be clearly shown that the drug and the drug delivery system do not follow the same kinetics, which is an important finding in the development of an optimized drug delivery system for a specific drug. Furthermore, while the general shape of the PK curve is similar between SPECT imaging and more traditional plasma measurements, which also means that the resulting C_{max} and T_{max} agree, one must be aware of the differences. For example,

Fig. 11. Comparison between ^{123}I-Fenofibrate and ^{125}I-Triolein SUV observations (symbols) with model predictions (lines) from the SPECT imaging study.

while the drug is traditionally analyzed in plasma, the measuring of the drug concentration in the heart is done in full blood, and thus at least a factor of (1 - hematocrit) smaller. This factor is important to calculate and compare the SUVs from the traditional and SPECT methods.

Overall, SPECT imaging of dual-labeled drug delivery systems is an excellent method for the piloting of new formulations. This approach might be especially useful for the evaluation of modern nanomedicines, e.g., drug filled liposomes, folate-targeted macromolecules, or lipid particles delivering RNA for vaccines and other personalized medicines.

Declaration of Competing Interest

The authors declare that they have no known competing financial interests or personal relationships that could have appeared to influence the work reported in this paper.

Acknowledgements

Appendix A. Supplementary material

Supplementary data to this article can be found online at https://doi.org/10.1016/j.ijpharm.2021.120884.

References

Adam, M.J., Wilbur, D.S., 2005. Radiohalogens for imaging and therapy. Chem. Soc. Rev. 34 (2), 153. https://doi.org/10.1039/b313872k.

Bailey, G.S., 1994. Labeling of peptides and proteins by radioiodination. Methods Mol. Biol. 32, 441–448.

Branderhorst, W., Vastenhouw, B., Beekman, F.J., 2010. Pixel-based subsets for rapid multi-pinhole SPECT reconstruction. Phys. Med. Biol. 55 (7), 2023–2034.

Caplan, S., Baniyash, M., 2002. Radioiodination of cellular proteins. Current protocols in cell biology Chapter 7, Unit 7 10.

Cavina, L., van der Born, D., Klaren, P.H.M., Feiters, M.C., Boerman, O.C., Rutjes, F.P.J. T., 2017. Design of Radioiodinated Pharmaceuticals: Structural Features Affecting Metabolic Stability towards *in Vivo* Deiodination. Eur. J. Org. Chem 2017 (24), 3387–3414.

Ceccarelli, C., Bianchi, F., Trippi, D., Brozzi, F., Di Martino, F., Santini, P., Elisei, R., Pinchera, A., 2004. Location of functioning metastases from differentiated thyroid carcinoma by simultaneous double isotope acquisition of I-131 whole body scan and bone scan. J. Endocrinol. Invest 27 (9), 866–869.

Chapman, M.J., 1987. Pharmacology of fenofibrate. Am. J. Med. 83 (5), 21–25.

Desager, J.P., Costermans, J., Verberckmoes, R., Harvengt, C., 1982. Effect of hemodialysis on plasma kinetics of fenofibrate in chronic renal failure. Nephron 31 (1), 51–54.

Dewaraja, Y.K., Ljungberg, M., Koral, K.F., 2000. Accuracy of 131I tumor quantification in radioimmunotherapy using SPECT imaging with an ultra-high-energy collimator: Monte Carlo study. J. Nucl. Med. 41, 1760–1767.

Esquinas, P., Rodríguez-Rodríguez, C., de la Vega, J., Bokharaei, M., Saatchi, K., Shirmohammad, M., Häfeli, U.O., Sossi, V., Celler, A., 2017. Re-188 image performance assessment using small animal multi-pinhole SPECT/PET/CT system. Physica Med. 33, 26–37.

Esquinas, P.L., Rodríguez-Rodríguez, C., Esposito, T.V.F., Harboe, J., Bergamo, M., Celler, A., Saatchi, K., Sossi, V., Häfeli, U.O., 2018. Dual SPECT Imaging of ^{111}In and ^{67}Ga to Simultaneously Determine In Vivo the Pharmacokinetics of Different Radiopharmaceuticals: A Quantitative Tool in Preclinical Research. Phys. Med. Biol. 63 (23), 235029. https://doi.org/10.1088/1361-6560/aaef63.

Gomes, C.M., Abrunhosa, A.J., Ramos, P., Pauwels, E.K.J., 2011. Molecular imaging with SPECT as a tool for drug development. Adv. Drug Delivery Rev. 63 (7), 547–554.

Goorden, M.C., van der Have, F., Kreuger, R., Ramakers, R.M., Vastenhouw, B., Burbach, J.P.H., Booij, J., Molthoff, C.F.M., Beekman, F.J., 2013. VECTor: a preclinical imaging system for simultaneous submillimeter SPECT and PET. J. Nucl. Med. 54 (2), 306–312.

Heo, J., Wolmer, I., Kegel, J., Iskandrian, A.S., 1994. Sequential Dual-Isotope Spect Imaging with Tl-201 and Technetium-99m-Sestamibi. J. Nucl. Med. 35, 549–553.

Hijnen, N.M., de Vries, A., Nicolay, K., Grüll, H., 2012. Dual-isotope 111In/177Lu SPECT imaging as a tool in molecular imaging tracer design. Contrast Media Mol. Imaging 7 (2), 214–222.

Hsieh, P.C., Lee, I.H., Yeh, T.L., Chen, K.C., Huang, H.C., Chen, P.S., Yang, Y.K., Yao, W. J., Lu, R.-B., Chiu, N.T., 2010. Distribution volume ratio of serotonin and dopamine transporters in euthymic patients with a history of major depression - a dual-isotope SPECT study. Psychiat. Res.-Neuroim. 184 (3), 157–161.

Ilovich, O., Qutaish, M., Hesterman, J.Y., Orcutt, K., Hoppin, J., Polyak, I., Seaman, M., Abu-Yousif, A.O., Cvet, D., Bradley, D.P., 2018. Dual-Isotope Cryoimaging Quantitative Autoradiography: Investigating Antibody-Drug Conjugate Distribution and Payload Delivery Through Imaging. J. Nucl. Med. 59 (9), 1461–1466.

Jeffrey, P., Burrows, M., Bye, A., 1987. Does the rat have an empty stomach after an overnight fast? Lab. Anim. 21 (4), 330–334.

Kevadiya, B.D., Chen, L., Zhang, L.u., Thomas, M.B., Davé, R.N., 2019. Fenofibrate Nanocrystal Composite Microparticles for Intestine-Specific Oral Drug Delivery System. Pharmaceuticals 12 (3), 109. https://doi.org/10.3390/ph12030109.

Khalil, M.M., 2011. Elements of Gamma Camera and SPECT Systems. In: Khalil, M.M. (Ed.), Basic Sciences of Nuclear Medicine. Springer, Berlin Heidelberg, Berlin, Heidelberg, pp. 155–178.

Kim, G.G., Poudel, B.K., Marasini, N., Lee, D.W., Hiep, T.T., Yang, K.Y., Kim, J.O., Yong, C.S., Choi, H.-G., 2013. Enhancement of oral bioavailability of fenofibrate by solid self-microemulsifying drug delivery systems. Drug Dev. Ind. Pharm. 39 (9), 1431–1438.

Lee, J., Coleman, R.E., Sherman, L.A., 1977. Comparison of iodine monochloride and modified chloramine-T radioiodination for in vivo protein studies. J. Lab. Clin. Med. 89, 836–844.

Lee, S., Gregor, J., Kennel, S.J., Osborne, D.R., Wall, J., Tian, J., 2015. GATE validation of standard dual energy corrections in small animal SPECT-CT. PLoS ONE 10 (4), e0122780.

Lee, S.Y., Gregor, J., Osborne, D., Wall, J., 2013. Dual Isotope SPECT Imaging of I-123 and I-125. Ieee Nucl Sci Conf R.

Liu, Z., Lin, K.-S., Bénard, F., Pourghiasian, M., Kiesewetter, D.O., Perrin, D.M., Chen, X., 2015. One-step (18)F labeling of biomolecules using organotrifluoroborates. Nat. Protoc. 10 (9), 1423–1432.

Loening, A.M., Gambhir, S.S., 2003. AMIDE: a free software tool for multimodality medical image analysis. Mol. Imaging 2 (3), 131–137.

Lui, B., Chang, J., Sun, J.S., Billings, J., Steves, A., Ackerhalt, R., Molnar, M., Kung, H.F., 1987. Radioactive iodine exchange reaction of HIPDM: kinetics and mechanism. J. Nucl. Med. 28, 360–365.

Markwell, M.A.K., 1982. A new solid-state reagent to iodinate proteins. I. Conditions for the efficient labeling of antiserum. Anal. Biochem. 125 (2), 427–432.

Michael Conlon, J., 2002. Preparation of 125I-Labeled Peptides and Proteins with High Specific Activity Using IODO-GEN. In: Walker, J.M. (Ed.), The Protein Protocols Handbook. Humana Press, Totowa, NJ, pp. 971–977.

Mock, B., Zheng, Q., 2006. Radiopharmaceutical chemistry: Iodination techniques. In: Henkin, R.E. (Ed.), Nuclear medicine, 2nd ed. Mosby Elsevier, Philadelphia.

NuDat, NuDat 2.8 database. Data source: National Nuclear Data Center, Brookhaven National Laboratory, based on ENSDF and the Nuclear Wallet Cards, available from (http://www.nndc.bnl.gov/nudat2/).

Ogawa, K., Harata, Y., Ichihara, T., Kubo, A., Hashimoto, S., 1991. A practical method for position-dependent Compton-scatter correction in single photon emission CT. IEEE Trans. Med. Imaging 10 (3), 408–412.

Pattison, G., 2019. Fluorination of organoboron compounds. Org. Biomol. Chem. 17 (23), 5651–5660.

Perkins, A.C., Frier, M., 2004. Radionuclide imaging in drug development. Curr. Pharm. Des. 10, 2907–2921.

Probst, R.J., Lim, J.M., Bird, D.N., Pole, G.L., Sato, A.K., Claybaugh, J.R., 2006. Gender differences in the blood volume of conscious Sprague-Dawley rats. J. Am. Ass. Lab. Animal Sci.: JAALAS 45, 49–52.

Robinson Jr., G.D., Lee, A.W., 1975. Radioiodinated fatty acids for heart imaging: iodine monochloride addition compared with iodide replacement labeling. J. Nucl. Med. 16, 17–21.

Rudin, M., Weissleder, R., 2003. Molecular imaging in drug discovery and development. Nat. Rev. Drug Discov. 2 (2), 123–131.

Schmitt, G.J., la Fougere, C., Dresel, S., Frodl, T., Hahn, K., Moller, H.J., Meisenzahl, E. M., 2008. Dual-isotope SPECT imaging of striatal dopamine: first episode, drug naive schizophrenic patients. Schizophr. Res. 101, 133–141.

Schumacher, T.N., Tsomides, T.J., 2001. *In vitro* radiolabeling of peptides and proteins. Curr Protoc Protein Sci Chapter 3, Unit 3 3.

Seevers, R.H., Counsell, R.E., 1982. Radioiodination Techniques for Small Organic-Molecules. Chem. Rev. 82 (6), 575–590.

SMITH, M.J., JOSEPH, J., FLATMAN, W.D., BASRAN, G.S., 1992. A Dual-Isotope Method for Studying Protein Kinetics in Pleural Effusions in Humans. Nucl. Med. Commun. 13 (6), 432–439.

Sonaje, K., Lin, K.-J., Wey, S.-P., Lin, C.-K., Yeh, T.-H., Nguyen, H.-N., Hsu, C.-W., Yen, T.-C., Juang, J.-H., Sung, H.-W., 2010. Biodistribution, pharmacodynamics and pharmacokinetics of insulin analogues in a rat model: Oral delivery using pH-Responsive nanoparticles vs. subcutaneous injection. Biomater. 31 (26), 6849–6858.

Sugiura, G., Kühn, H., Sauter, M., Haberkorn, U., Mier, W., 2014. Radiolabeling strategies for tumor-targeting proteinaceous drugs. Molecules 19 (2), 2135–2165.

Sutherland, D., 2019. Radiohalogenation of Organic Compounds: Practical Considerations and Challenges for Molecular Imaging. Synthesis-Stuttgart 51 (23), 4368–4373.

Szpera, R., Moseley, D.F.J., Smith, L.B., Sterling, A.J., Gouverneur, V., 2019. The Fluorination of C-H Bonds: Developments and Perspectives. Angew. Chem. Int. Ed. Engl. 58 (42), 14824–14848.

Tran, T., Bønløkke, P., Rodríguez-Rodríguez, C., Nosrati, Z., Esquinas, P.L., Borkar, N., Plum, J., Strindberg, S., Karagiozov, S., Rades, T., Müllertz, A., Saatchi, K., Häfeli, U. O., 2020. Using *in vitro* lipolysis and SPECT/CT *in vivo* imaging to understand oral absorption of fenofibrate from lipid-based drug delivery systems. J. Control Release 317, 375–384.

Tsartsalis, S., Tournier, B.B., Habiby, S., Ben Hamadi, M., Barca, C., Ginovart, N., Millet, P., 2018. Dual-radiotracer translational SPECT neuroimaging. Comparison of three methods for the simultaneous brain imaging of D2/3 and 5-HT2A receptors. Neuroimage 176, 528–540.

Tsuji, A., Kojima, A., Matsumoto, M., Oyama, Y., Tomiguchi, S., Kira, T., Takagi, Y., Shimomura, O., Takahashi, M., 1999. A new method for crosstalk correction in simultaneous dual-isotope myocardial imaging with T1–201 and I-123. Ann. Nucl. Med. 13, 317–323.

Uhrig, M.L., Lantaño, B., Postigo, A.l., 2019. Synthetic strategies for fluorination of carbohydrates. Org. Biomol. Chem. 17 (21), 5173–5189.

Vaidyanathan, G., Zalutsky, M.R., 2019. In: Radiopharmaceutical Chemistry. Springer International Publishing, Cham, pp. 391–408. https://doi.org/10.1007/978-3-319-98947-1_22.

van der Have, F., Vastenhouw, B., Ramakers, R.M., Branderhorst, W., Krah, J.O., Ji, C., Staelens, S.G., Beekman, F.J., 2009. U-SPECT-II: An Ultra-High-Resolution Device for Molecular Small-Animal Imaging. J Nucl. Med. 50 (4), 599–605.

Vanderheyden, J.L., 2009. The use of imaging in preclinical drug development. Q. J. Nucl. Med. Mol. Im. 53, 374–381.

Wilbur, D.S., 1992. Radiohalogenation of proteins: An overview of radionuclides, labeling methods and reagents for conjugate labeling. Bioconj. Chem. 3 (6), 433–470.

Willmann, J.K., van Bruggen, N., Dinkelborg, L.M., Gambhir, S.S., 2008. Molecular imaging in drug development. Nat. Rev. Drug. Discov. 7 (7), 591–607.

Zaidi, H., Hasegawa, B., 2003. Determination of the attenuation map in emission tomography. J. Nucl. Med. 44, 291–315.

Zaidi, H., Koral, K.F., 2004. Scatter modelling and compensation in emission tomography. Eur. J. Nucl. Med. Mol. Imaging 31 (5), 761–782.

Zhu, X.P., Park, M.A., Gerbaudo, V.H., Moore, S.C., 2007. Quantitative simultaneous In-111/Tc-99m planar imaging in a long-bone infection phantom. Physics in Medicine and Biology 52, 7353-7365.